

Article

Not peer-reviewed version

---

# Morphology and Mechanics of Star Copolymer Films Probed by AFM in Air and in Liquid

---

[Cristiano Albonetti](#) \* , [Lorella Izzo](#) , [Giovanni Vigliotta](#) , Matilde Sublimi Saponetti , Fabiola Liscio , [Fabrizio Bobba](#)

Posted Date: 21 December 2023

doi: 10.20944/preprints202312.1596.v1

Keywords: star copolymers; films; morphology; mechanical properties; <span>AFM</span>; force volume maps



Preprints.org is a free multidiscipline platform providing preprint service that is dedicated to making early versions of research outputs permanently available and citable. Preprints posted at Preprints.org appear in Web of Science, Crossref, Google Scholar, Scilit, Europe PMC.

Copyright: This is an open access article distributed under the Creative Commons Attribution License which permits unrestricted use, distribution, and reproduction in any medium, provided the original work is properly cited.

Disclaimer/Publisher's Note: The statements, opinions, and data contained in all publications are solely those of the individual author(s) and contributor(s) and not of MDPI and/or the editor(s). MDPI and/or the editor(s) disclaim responsibility for any injury to people or property resulting from any ideas, methods, instructions, or products referred to in the content.

## Article

# Morphology and Mechanics of Star Copolymer Films Probed by AFM in Air and in Liquid

Cristiano Albonetti <sup>1,2,\*</sup>, Lorella Izzo <sup>3,4</sup>, Giovanni Vigliotta <sup>4</sup>, Matilde Sublimi Saponetti <sup>5</sup>, Fabiola Liscio <sup>6</sup> and Fabrizio Bobba <sup>2,5</sup>

<sup>1</sup> Consiglio Nazionale delle Ricerche - Istituto per lo Studio dei Materiali Nanostrutturati (CNR-ISMN), Via P. Gobetti 101, 40129 Bologna, Italy; cristiano.albonetti@cnr.it

<sup>2</sup> Consiglio Nazionale delle Ricerche - Istituto superconduttori, materiali innovativi e dispositivi (CNR-SPIN), Via Giovanni Paolo II, 132 - 84084 Fisciano, Salerno, Italy; cristiano.albonetti@cnr.it

<sup>3</sup> Dipartimento di Biotecnologie e Scienze della Vita, Università degli Studi dell'Insubria, Via J.H. Dunant, 3, 21100 Varese, Italy; lorella.izzo@uninsubria.it

<sup>4</sup> Dipartimento di Chimica e Biologia "A. Zambelli", Università degli Studi di Salerno, Via Giovanni Paolo II, 132, 84084 Fisciano, Salerno, Italy; gvigliotta@unisa.it

<sup>5</sup> Dipartimento di Fisica "E.R. Caianiello", Università degli Studi di Salerno, Via Giovanni Paolo II, 132, 84084 Fisciano, Salerno, Italy; fbobba@unisa.it

<sup>6</sup> Consiglio Nazionale delle Ricerche - Istituto per la Microelettronica e i Microsistemi (CNR-IMM), Via P. Gobetti 101, Bologna 40129, Italy; liscio@bo.imm.cnr.it

\* Correspondence: cristiano.albonetti@cnr.it

**Abstract:** Star copolymer films were studied for confirming the role of film morphology in antimicrobial activity previously reported. With this scope, films of a two-branches copolymer, namely m-PEG-(MMA-ran-DMAEMA)<sub>2</sub>, containing  $\approx 40$  % in mol of non-quaternized 2-(dimethylamino)ethyl methacrylate, were produced by using spin-coating, drop-casting and casting deposition techniques, thus obtaining ultra-thin, thin and thick films, respectively. The morphology is generally flat for thin and thick films, but it becomes substrate dependent for ultra-thin films where the film planarization effect is not efficient. Mechanical properties of such films were investigated by Force Volume Maps in both air and liquid. In air, ultra-thin films are in the substrate-dominated zone and thus the elastic modulus  $E$  is overestimated, while  $E$  reaches its bulk value for thin and thick films. In liquid (water),  $E$  follows an exponential decay for all films with a minimum soaked time  $t_0$  of 0.37 and 2.65 h for ultra-thin and thin and thick films, respectively. After this time,  $E$  saturates to a value in average 92 % smaller than that measured in air due to films swelling. Such results confirm the role of morphology envisaged in literature, suggesting also an additional role of mechanical properties in the antimicrobial activity.

**Keywords:** star copolymers; films; morphology; mechanical properties; AFM; Force Volume Maps

## 1. Introduction

Star copolymers have the ability to form films with physical properties modulated by their topology [1–3], albeit those films are usually amorphous or semi-crystalline due to the low degree of crystallinity of star copolymers [2,4]. Amongst their possible applications, biomedical uses are intensely investigated to date [5]. For instance, the antimicrobial activity of films was recently increased by synthesizing novel star copolymers [6,7], surpassing the drop of the capacity to kill bacteria over time obtained with other antimicrobial strategies [8,9]. The best results were obtained with two-branches copolymers, namely m-PEG-(MMA-ran-DMAEMA)<sub>2</sub>, insoluble in water and containing  $\approx 40$  % in mol of non-quaternized 2-(dimethylamino)ethyl methacrylate (DMAEMA), from which films were prepared. Such efficient antimicrobial activity was mainly attributed to enhanced protonation of DMAEMA pendants sustained by the dimerization of vicinal ammonium/amino groups [6,7,10–12]. Authors suggest also a morphological explanation for the increased antimicrobial



activity, ascribable to the "...volume of internal cavities or channels. The latter idea finds strong support in the water uptake data and in the  $T_g$  (glass transition temperature) values after sorption of water, indicating a less compact of the  $A(BC)_2$  (two-branches copolymers) structure" [6].

This work aims to study morphological and mechanical aspects of m-PEG-(MMA-ran-DMAEMA)<sub>2</sub> films by modulating both the substrate where films are deposited and their thicknesses. Morphological and mechanical measurements were performed in air and in liquid, and compared to films with high antimicrobial activity analyzed in Ref. [6,7].

## 2. Materials and Methods

### 2.1. Polymeric materials

The star copolymer m-PEG-(MMA-ran-DMAEMA)<sub>n</sub> with  $n = 2$  was synthesized at 70 °C in toluene [6]. A 50 ml glass flask was charged, under nitrogen atmosphere, with 0.1 g of m-PEG-Br<sub>2</sub> macro initiator and 15 ml of dry toluene. After the dissolution of the macroinitiator, 0.03 g of CuBr, 0.05 g of bpy, 5 ml of MMA, and 2.5 ml of DMAEMA were added. The mixture, maintained at 70 °C, was magnetically stirred for 18 h and then the reaction was stopped with n-hexane. The copolymer was recovered, dissolved in the minimum amount of chloroform, and passed over a column of activated Al<sub>2</sub>O<sub>3</sub> to remove the catalyst. The solution was dried in vacuum, the copolymer was recovered, washed with cold methanol, and then dried in vacuum. As measured by Gel Permeation Chromatography, the copolymer molecular weight,  $M_n$ , and its polydispersity index, PDI, are 89 kDa and 1.4, respectively.

From now on, m-PEG-(MMA-ran-DMAEMA)<sub>2</sub> is briefly termed A(BC)<sub>2</sub> where the block A, m-PEG, is bound to the two blocks BC composed of methylmethacrylate (MMA) and nonquaternized 2-(dimethylamino)ethyl methacrylate (DMAEMA).

The A(BC)<sub>2</sub> powder was dissolved in chloroform (CHCl<sub>3</sub>) in order to obtain two solutions with concentrations  $c$  of 1 and 4 mg·ml<sup>-1</sup> and polymer mass fraction  $wt\%$  of 0.067 and 0.268, respectively (see Supplementary Materials).

### 2.2. Silicon substrates

Substrates are  $\approx 1 \times 1$  cm<sup>2</sup> chips prepared by cleaving manually a Si (111) wafer coated with native SiO<sub>x</sub> ( $p$ -type,  $\rho = 10 \Omega \cdot \text{cm}$ ) [13]. Both sides of the Si wafer were mechanically polished (MP), obtaining optically specular surfaces. Finally, one side was finished by chemical mechanical polishing (CMP), obtaining an atomically flat defect-free surface [14]. Before their use, substrates are cleaned by acetone vapors to remove possible physical/chemical contaminants.

### 2.3. Preparation of ultra-thin polymeric films by spin-coating

Ultra-thin polymeric films were prepared spun-coating 300  $\mu\text{l}$  of A(BC)<sub>2</sub> solution ( $c = 1 \text{ mg} \cdot \text{ml}^{-1}$ ) on silicon substrates. The spin process consists of two steps: i) the solution was deposited on the substrate by using a mechanical air-cushion pipette (100 – 1000  $\mu\text{l}$ , Eppendorf Research, Stevenage, UK) placed near the substrate surface ( $\approx 2$  cm). In order to obtain a homogeneous fluid film on the substrate surface, the solution was deposited after the acceleration stage of the spin-coater when the final rotational speed  $\omega$  is reached (specifically,  $\omega$  is 3000, 3200, 3500, 3750 and 4000 rpm) [15]; and ii) the fluid film is gradually thinned up to its final thickness  $h_w$  by keeping the rotational speed  $\omega$  for additional 10 s.

Spin-coated samples were closed within plastic petri dishes and placed under a chemical hood for 20 h in order to evaporate completely CHCl<sub>3</sub> at room temperature from the fluid film and thus obtain solid, transparent, and insoluble (in water) ultra-thin films [16].

The final thickness  $h_f$  when the film is solid increases with  $c$  and decreases with  $\omega$ , depending also on the adopted solvent [17]. Since  $c$  was assumed constant during the spin-coating process,  $h_f$  can be evaluated by using Meyerhofer's equation [18]:

$$h_f = wt\% \cdot h_w = wt\% \cdot \left[ \left( \frac{3\eta_0}{2\rho} \right) \cdot \frac{k}{(1-wt\%)} \right]^{1/3} \cdot \omega^{-2/3}, \quad (1)$$

where  $k$  is the mass transfer coefficient, i.e. the amount of polymer transferred from the solution to the substrate [19],  $\eta_0$  (in cgs,  $cP = 10^{-2} \text{ g}\cdot\text{cm}^{-1}\cdot\text{s}^{-1}$ ) is the solution viscosity and  $\rho$  (in  $\text{g}\cdot\text{cm}^{-3}$ ) is its density.

The high rotational speeds adopted herein ( $\omega \geq 3000$  rpm) should produce ultra-thin films with  $h_f$  almost independent of  $\omega$  [23]. To confirm this,  $h_f$  calculated from Equation 1 needs additional physical parameters characterizing the  $\text{A}(\text{BC})_2$  solution (see Table 1). Since  $\eta_0$  and  $\rho$  are unknown for  $\text{A}(\text{BC})_2$ , they are assumed equal to those obtained for the polymer MEH-PV which has similar  $M_n$ , 86 kDa, and PDI, 1.52 (MEH-PV is also dissolved in  $\text{CHCl}_3$ ) [23]. Specifically, the  $\text{A}(\text{BC})_2$  solution has  $\rho = 0.99 \text{ g}\cdot\text{cm}^{-3}$  and  $\eta_0 \approx 0.61 \text{ cP} = 0.61 \cdot 10^{-2} \text{ g}\cdot\text{cm}^{-1}\cdot\text{s}^{-1}$  for  $wt\% = 0.067$  (see Supplementary Materials). The first term in the cube root of Equation 1, i.e.  $3\eta_0/2\rho$ , is  $\approx 0.92 \cdot 10^{-2} \text{ cm}^2\cdot\text{s}^{-1}$ , while the second term  $k$  is  $\approx 1.25 \cdot 10^{-9} \text{ cm}\cdot\text{s}^{-1/2}$  (as calculated from Equation 8 of Ref. [20] with data of Table 1), so the cube root of Equation 1 is  $\approx 2.3 \cdot 10^{-4} \text{ cm}\cdot\text{s}^{-1/2}$ . Accordingly,  $h_f$  ranges from  $\approx 11$  to  $\approx 9$  nm for  $\omega = 3000$  and 4000 rpm, respectively (rpm was expressed in Hz for dimensional analysis, by using the equivalence 1 rpm = 1/60 Hz). These calculated thicknesses confirm the slight dependence of  $h_f$  vs.  $\omega$  for high rotational speeds.

**Table 1.** Physical parameters of the  $\text{A}(\text{BC})_2$  solution useful to calculate  $k$  from Equation 8 of Ref. [20].

A( $\text{BC}$ ) <sub>2</sub> data
$T = 298.15 \text{ K}$
$R = 82.06 \text{ atm}\cdot\text{cm}^3\cdot\text{mol}^{-1}\cdot\text{K}^{-1}$
$D_g = 0.106 \cdot 10^{-6} \text{ cm}^2\cdot\text{s}^{-1}$ a
$\nu_g = 0.1553 \text{ cSt} = 0.1553 \cdot 10^{-2} \text{ cm}^2\cdot\text{s}^{-1}$ b
$P_{\text{CHCl}_3} = 26.271 \text{ kPa} \approx 0.26 \text{ atm}$ c
$M_{\text{CHCl}_3} = 119.38 \text{ g}\cdot\text{mol}^{-1}$ d
$\rho_0 = 1.49 \text{ g}\cdot\text{cm}^{-3}$ e
$C = 0.5474$ f

a  $D_g$  is the binary diffusivity of the solvent in the overhead gas phase [21]; b  $\nu_g$  is the kinematic viscosity of the overlying gas [21]; c  $P_{\text{CHCl}_3}$  is the vapor pressure of pure chloroform ( $\text{CHCl}_3$ ) at temperature  $T$  [22]; d  $M_{\text{CHCl}_3}$  is the molecular weight of chloroform; e  $\rho_0$  is the density of pure chloroform; f C depends on the Schmidt number of the overlying gas [20,21].

#### 2.4. Preparation of thin and thick polymer films by drop-casting and casting

Thin and thick polymeric films were prepared by drop-casting [24]. Thin films,  $\approx 200$  nm thick, were obtained by depositing 1 ml of solution on a TEM grid (mesh 300) placed on CMP substrates. Samples were placed within a Teflon Petri dish under a chemical hood for 24 h so as to evaporate completely  $\text{CHCl}_3$  at room temperature. Thick films,  $\approx 400 \mu\text{m}$  thick, are self-standing films prepared by dissolving 200 mg of copolymer in 50 ml of  $\text{CHCl}_3$  at room temperature, i.e.  $c = 4 \text{ mg}\cdot\text{ml}^{-1}$ . The solution was cast in a Teflon Petri dish (diameter 3 cm), and the solvent was evaporated at room temperature. The film was removed from the Petri dish and stored in a vacuum oven at 30 °C for three days [7]. Self-standing polymeric films are prepared in the same way reported in the literature [12] and used as data reference.

#### 2.5. X-ray reflectivity measurements

X-ray reflectivity (XRR) measurements were performed using a SmartLab-Rigaku diffractometer equipped with a rotating anode ( $\text{Cu K}\alpha$ ,  $\lambda = 1.54180 \text{ \AA}$ ), followed by a parabolic mirror to collimate the incident beam and a series of variable slits (placed before and after the sample position) to reach an acceptance of 0.01°.

#### 2.6. Atomic Force Microscopy imaging

The microscope used for all measurements was a JPK Nanowizard III equipped with Vortex electronics (Bruker Nano GmbH, Berlin, DE). All polymeric films were firstly topographically investigated by using the amplitude modulation atomic force microscopy technique (AM-AFM) under ambient conditions. All three available MikroMash NSC35 cantilevers with nominal resonant frequency  $\omega_0$  of  $\approx 150$ ,  $\approx 200$  and  $\approx 300$  kHz and correspondent nominal spring constant  $k$  of  $\approx 6$ ,  $\approx 9$  and  $\approx 16$  N·m $^{-1}$  were employed for AM-AFM (when necessary, the real  $k$  was calculated through the Sader method [25]).

The mechanical properties of the polymeric films were evaluated by Force Volume Maps (FVM) obtained by using the Quantitative Imaging (QI) mode developed by JPK Instruments [26]. In FVM mode, multiple force curves are acquired at points (pixel, px) of a defined grid pattern of 128 x 128 px $^2$  for our experiments. The interactions between the tip and sample are measured locally and mapped point-by-point for a defined 3D region using force-distance curves. In particular, the tip is moved towards (approach curve) and away from (retraction curve) the sample surface at each point of the grid pattern, while the cantilever deflection (in V) is continually registered with respect to the position of the piezoelectric actuator (in  $\mu\text{m}$ , termed "height") [27]. Prior measurements, the elastic constant  $k$  of the cantilever was calibrated in air on bare thermal SiO<sub>2</sub> substrate by performing a force curve on a single point of the SiO<sub>2</sub> surface [28]. The slope of the linear part after the jump-to-contact point is reciprocal to the cantilever sensitivity  $s$  (in nm·V $^{-1}$ ) and is useful to convert in nm the cantilever deflection measured from the photodiode (in V). Once measured  $s$ ,  $k$  was calculated by using the thermal tune method (see Supplementary Materials of Ref. [29]). FVMs were obtained by fixing the maximum applied force  $F_{\max}$  (in nN) calculated from Hook's law  $k \cdot U \cdot s$ , where the cantilever deflection  $U$  (in V) was kept constant at 0.5 V for all measurements [30]. Force curves composing the FVM have a fixed maximum path length of 50 nm, which is travelled in 200 ms (approach and retraction paths). QI experiments were performed in both air and liquid (mQ water) where, in liquid, the sample was placed in the centre of a home-made pool built by fixing a polypropylene tube 5 mm long (outer diameter  $\varnothing = 24$  mm, inner  $\varnothing = 23$  mm) on a glass microscope slide. Both the tube and sample were fixed on the glass slide by using the JPK bio-compatible glue [31]. The total volume of the pool is about 1.5 mL, which grants up to 8 hours of consecutive measurements (for longer measurements the pool was refilled). QI measurements employed Bruker RTESP, LTESP and MikroMash NSC35 silicon cantilevers with  $\omega_0 \approx 180$ , 190 and  $\approx 290$  kHz, respectively, and calibrated elastic constants  $k$  of  $\approx 35$ ,  $\approx 46$ ,  $\approx 32$  N·m $^{-1}$ .

Topographic images were analyzed with the software Gwyddion [32], while QI images by the JPK Data Processing software (version spm-5.1.8).

### 3. Results and Discussions

#### 3.1. Morphological characterization of silicon substrates

The morphology of wafer sides surfaces, i.e. mechanical polished (MP) and chemical mechanical polished (CMP), are characterized by AM-AFM. The MP surface shows features in the order of tens of nm due to mechanical finishing (see Figure 1a), while the CMP surface is flat with details below a nm (see Figure 1b). Accordingly, the root mean square roughness  $R_q$  reduces from  $(10.7 \pm 1.2)$  to  $(0.10 \pm 0.025)$  nm for MP and CMP, respectively.

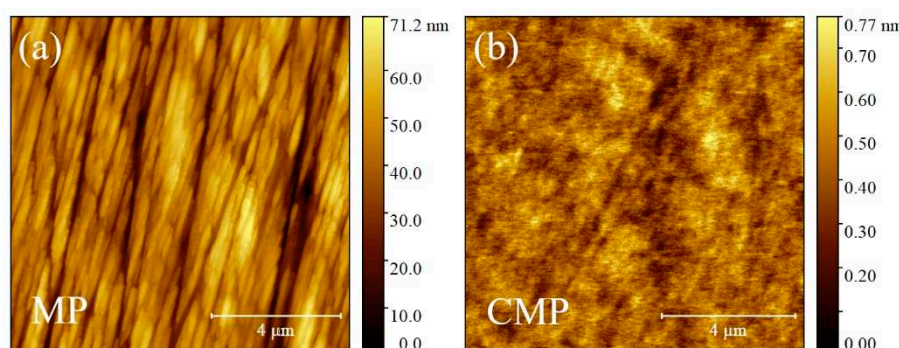


**Figure 1.** Topographic AFM images  $10 \times 10 \mu\text{m}^2$  of mechanical (a, MP) and chemical mechanical (b, CMP) polished wafer surfaces. The maximum value of false color map ruler is reduced by two orders of magnitude from MP to CMP, stressing roughness differences.

Such  $R_q$  values are comparable to those reported in the literature [33] where CMP wafers were polished with different abrasive SiC papers and velvet rugs imbued with  $\text{Al}_2\text{O}_3$  slurry for assessing the evolution of the roughness parameters vs. progressively finer polishing. The  $R_q$  value of the MP side is consistent with a surface polished by SiC papers with a grit higher than 400 (possibly 1200 [34]), while the CMP side has an  $R_q$  value even lower than that reported in the literature and defined “not machined surfaces” [33] due to a higher cleanliness (compare Figure 1b and Figure 1d of Ref. [33]).

To evaluate roughness parameters of the MP surface, a one-dimensional analysis of averaged topographic profiles is used [32,35]. The average profile is obtained by averaging 90 adjacent profile lines along the direction orthogonal to polishing features. Then, one-dimensional analysis splits the averaged topographic profile into waviness (the low-frequency components, correspondent to the polynomial background of the image) and roughness (the high-frequency components) [36]. Such analysis measures a sort of surface oscillations with specific amplitudes and wavelengths albeit, in principle, the MP surface has a non-periodic profile (see Supplementary Materials). Such a splitting procedure depends critically on the cut-off  $C$  that, set to 0.0098, correctly splits the MP surface profile (see Figure 2 and C calculations in Supplementary Materials).

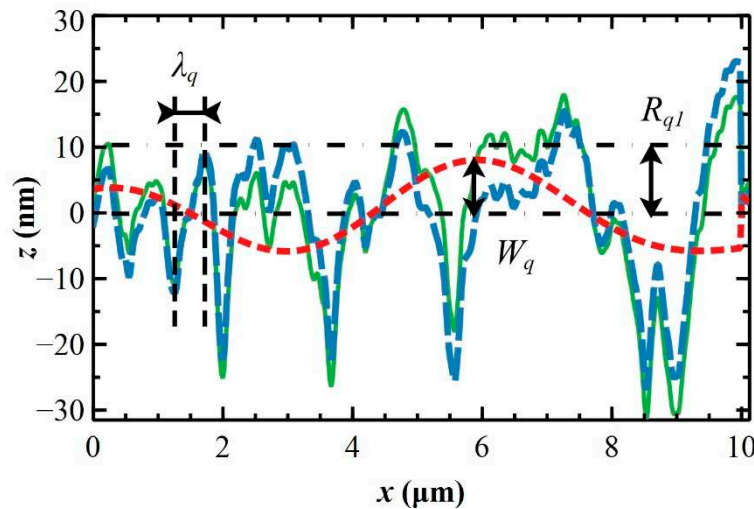


**Figure 2.** Typical topographic profile in the  $z - x$  plane,  $z$  is the height variations and  $x$  is the direction orthogonal to polishing features, obtained by averaging 90 adjacent profiles from MP AFM images (continuous green line). One-dimensional analysis splits the profile into waviness (red fine dashed line) and roughness (blue dashed line) profiles that are characterized by an average amplitude  $W_q$  and wavelength  $\lambda_q$  and a root mean square roughness  $R_{q1}$ , respectively.

The profile of the surface roughness obtained by one-dimensional analysis on  $10 \times 10 \mu\text{m}^2$  topographic images (blue dashed line in Figure 2) has a roughness  $R_{q1}$  of  $(8.5 \pm 0.1) \text{ nm}$  and a root mean square wavelength  $\lambda_q$ , i.e. the average peak-to-valley distance [37], of  $(0.72 \pm 0.03) \mu\text{m}$ . The waviness, the red dashed line in Figure 2, is characterized by a root mean square amplitude  $W_q$  of  $(1.8 \pm 0.6) \text{ nm}$ . Adding  $W_q$  to  $R_{q1}$  gives a result of  $(10.3 \pm 0.7) \text{ nm}$  that is equal, within experimental error, to the roughness  $R_q$  calculated from the height distribution [38].

### 3.2. X-ray characterization of ultra-thin and thin polymeric films

Two distinct behaviors are clearly visible in XRR curves on MP and CMP substrates (see Figure 3). Polymeric films deposited on CMP substrates, at  $\omega = 3000$  and  $3200 \text{ rpm}$ , exhibit Kiessig fringes generated by the constructive interference of the reflected X-ray beam by both the polymeric film surface and the film/substrate interface [39]. Such fringes are indicative of a smooth film surface and

a smooth film/substrate interface, in agreement with data obtained by AFM. The thickness of the polymeric films can be estimated from Kiessig periodicity, obtaining an estimated range of [10,12] nm for both films. Notably, such thickness values are similar to those theoretically calculated in Section 2.3. The reduction of Kiessig amplitude intensity for the film deposited at  $\omega = 3000$  rpm indicates an increased roughness of the film surface with respect to that deposited at  $\omega = 3200$  rpm, in line with the smoothing effect expected for increasing  $\omega$  on films deposited on CMP substrates. Conversely, XRR curves of polymeric films deposited on MP substrates at  $\omega$  ranging from 3500 to 4000 rpm do not show Kiessig fringes and the XRR signal is damped. This is typical of ultra-thin films deposited on (relatively) rough surfaces [40], as observed by AFM.

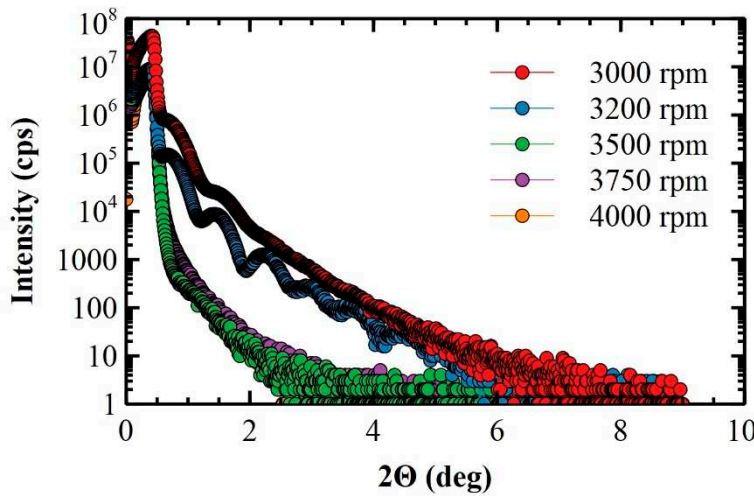


**Figure 3.** XRR scans of ultra-thin polymeric films deposited on CMP and MP substrates at 3000, 3200 rpm and 3500, 3750, 4000 rpm, respectively.

### 3.3. Morphological characterization of ultra-thin, thin and self-standing polymeric films

The morphology of polymeric films depends strongly on the deposition technique.

In spin-coated films, it depends on the substrate, CMP or MP, and the rotational speed  $\omega$ . This latter dependence is lost in the case of CMP substrates where films are flat with an average roughness  $R_q$  of  $\approx 0.17$  nm (see Table 2) and featureless even at large scale (see Figure 4a and its inset).

**Table 2.** Surface roughness parameters obtained by one-dimensional analysis of polymeric films deposited on MP and CMP substrates.

$\omega$ (rpm)	Sub	$R_q$ (nm)	$W_a$ (nm)	$\lambda a$ ( $\mu$ m)	$R_{q1}$ (nm)	$s_h$ (nm)	$P$ (%)
3000	CMP	$0.15 \pm 0.025$	/	/	/	$\approx 0.14$	$\approx 100$
3200	CMP	$0.19 \pm 0.125$	/	/	/	$\approx 0.19$	$\approx 100$
3500	MP	$6.4 \pm 0.4$	$2.5 \pm 1.9$	$0.60 \pm 0.15$	$4.1 \pm 0.8$	$18 \pm 3$	$49 \pm 17$
3750	MP	$4.5 \pm 0.9$	$2.1 \pm 0.7$	$0.98 \pm 0.36$	$3.0 \pm 1.3$	$13 \pm 3$	$63 \pm 25$
4000	MP	$4.0 \pm 0.5$	$1.2 \pm 0.2$	$0.65 \pm 0.29$	$2.6 \pm 0.4$	$9.3 \pm 0.1$	$73 \pm 13$

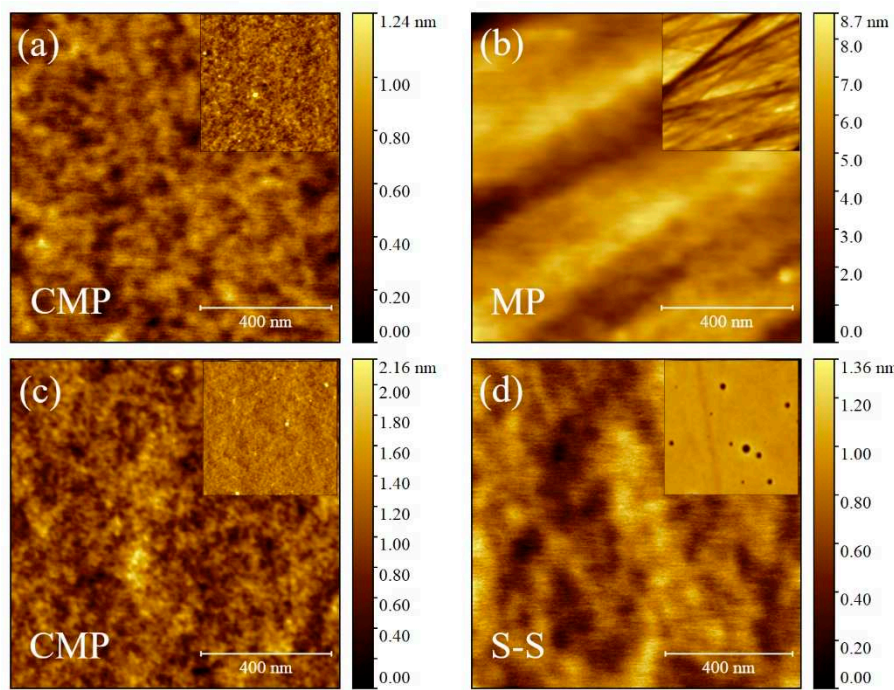


**Figure 4.** Topographic AFM images of polymeric films deposited by: (i) spin-coating on CMP (a) and MP (b) substrates at 3200 and 4000 rpm, respectively; (ii) drop-casting on CMP substrates (c); and (iii) self-standing films, S-S, obtained by casting (d). All images are  $1 \times 1 \mu\text{m}^2$ . Insets: Topographic images at larger scale ( $3.5 \times 3.5 \mu\text{m}^2$ ) to show morphological features of films (a) or their flatness (b – d).

Otherwise the film morphology depends on  $\omega$  due to the morphology of MP substrates (see Figure 4b). By comparing Figures 1a and 4b, polymeric films clearly smooth the topographical features of bare MP substrates, although relatively large scratches are still present. The roughness of polymeric films, measured both by one-dimensional analysis,  $R_{q1}$  as well as height distribution,  $R_q$ , are progressively reduced vs.  $\omega$  from  $R_{q1} \approx 4.1$  to  $\approx 2.6$  nm for 3500 and 4000 rpm, respectively (see Table 2). Such a reduction, but less pronounced, is also observed on  $W_q$ . Within experimental errors,  $\lambda_q$  remains, on average, constant at  $(0.74 \pm 0.30) \mu\text{m}$  and independent of  $\omega$  (see Table 2).

For understanding the morphological evolution of polymeric films vs.  $\omega$ , one-dimensional parameters summarized in Table 2 are compared with those obtained on bare MP substrates ( $\lambda_q \approx 0.72 \mu\text{m}$ ,  $W_q \approx 1.8$  nm and  $R_{q1} \approx 8.5$  nm). The wavelength  $\lambda_q$ , which is determined by surface scratches, is unaffected by the presence of films and invariant with  $\omega$ . Since scratches are deeper, or at most comparable, to the film thickness  $h_f$  (in average  $\approx 11$  nm, cp. to Section 3.2), their modulations are preserved even after the film deposition. results. The amplitude  $W_q$  also depends on scratches, but it is reduced with respect to the bare MP substrate for films deposited at  $\omega = 4000$  rpm. The roughness  $R_{q1}$  is lower than the roughness of the bare MP substrate, also for increasing  $\omega$ . Since  $R_{q1}$  is governed by small height variations around the oscillating roughness profile (see Figure 2), its reduction means that such height modulations are progressively filled by the film for increasing rotational speed  $\omega$ .

These experimental observations can be rationalized with a single parameter termed surface planarization  $P$  (in %) [41]. Mathematically,  $P$  is defined as:

$$P = 100 \left[ 1 - \frac{s_h}{d} \right], \quad (2)$$

where  $s_h$  and  $d$  are the (average) peak-to-valley roughness, *viz.*  $R_z$  (ISO) [42], for the polymeric film and the bare MP substrate, respectively. If the film is conformal to substrate features,  $s_h \rightarrow d$  and  $P \rightarrow 0\%$ . Vice versa, if the film is flat  $s_h \rightarrow 0$  and  $P \rightarrow 100\%$ . For bare MP substrates,  $d$  is  $(35 \pm 6)$  nm and  $s_h$  ranges from  $\approx 18$  to  $\approx 9$  nm for 3500 and 4000 rpm, respectively (see Table 2). Accordingly,  $P$  runs from  $\approx 49$  to  $\approx 73\%$ . In the case of spin-coated films on CMP substrates, they are flat with a small  $d$  of  $(0.15 \pm 0.05) \text{ \AA}$ . The same for  $s_h$  that is  $\approx 0.15$  nm and  $\approx 0.2$  nm for 3000 and 3200 rpm, respectively (see

Table 2). Substrates and films have comparable  $R_z$  (ISO), so films are flat ( $P = 100\%$ ) as well as the CMP substrate.

Polymeric films on CMP substrates deposited by drop-casting are flat and featureless with an  $R_q$  of  $(0.25 \pm 0.025)$  nm, even at large scale size (see Figure 4c and its inset). Similarly, self-standing polymeric films S-S have a surface roughness  $R_q$  of  $(0.20 \pm 0.025)$  nm (see Figure 4c and its inset).

In view of the  $P$  values reported in Table 2, MP substrate planarization through the polymeric film is affected by both substrate corrugations and  $\omega$ . Such nanometer corrugations are also expected to locally change the film thickness.

The fluid film formed on the substrate surface during the spin-coating deposition is pivotal for the planarization effect. The  $A(BC)_2$  solution is a non-Newtonian fluid due to the high volatility of  $CHCl_3$  and, also, it is a low viscosity fluid due to the low concentration of the solution ( $c = 1 \text{ mg}\cdot\text{ml}^{-1}$ ) and the low polymer mass fraction dissolved in  $CHCl_3$  ( $wt\% = 0.067$ ). Such a fluid easily fills completely scratches independently of  $\omega$  [43]. Such filling is also facilitated by the average width of scratches (few hundreds of nm); indeed, the lowest critical width at which trench filling is impeded is about 5 cm (as calculated from the spin-coating theory in our experimental conditions [44]), several orders of magnitude larger than the average width of scratches. Accordingly, the liquid film spin-coated on the substrate fills the scratches completely and, after solvent evaporation, surface planarization is obtained although it will be not perfect due to the non-Newtonian behavior of the solution [44].

The (relatively) flat regions between scratches show a different behavior. The liquid film thickness  $h_w$  is thinned for increasing  $\omega$  similarly to flat substrate like CMP. The solid film thickness  $h_f$  is reduced from 10 to 9 nm passing from  $\omega = 3500$  to 4000 rpm (cp. Section 2.3), a thickness comparable to small height variations determining  $R_{q1}$  ( $\approx 8.5$  nm). In these conditions, height variations are smoothed by the film [45,46] and  $R_{q1}$  is reduced from  $\approx 8.5$  nm (bare substrate) to  $\approx 4.1$  nm or less (see Table 2). The liquid film spin-coated on the substrate is governed by capillary forces ( $\Omega^2 \approx 10^{-7}$  [47]) and the solution moves towards roughness valleys ( $\approx 100$  nm wide, as evaluated by Height-Height Correlation Function [48]) rather than on top of hills due to their high aspect ratio [49]. Since  $h_f$  is larger for lower  $\omega$ , the dried film on roughness hills,  $h_f(H)$ , will be thicker at 3500 to 4000 rpm while the roughness valleys, like scratches, will be filled completely by the solution and  $h_f(V)$  will be independent to  $\omega$  (see Figure 5a,b). Consequently,  $h_f(H)$  obtained at  $\omega_1$ ,  $h_f(H)|_{\omega_1}$ , is thicker than  $h_f(H)|_{\omega_2}$  if  $\omega_1 < \omega_2$  while  $h_f(V)|_{\omega_1} = h_f(V)|_{\omega_2}$  regardless  $\omega$ . As reported by Table 2,  $R_{q1}|_{\omega_1} > R_{q1}|_{\omega_2}$  for  $\omega_1 < \omega_2$ , explaining why  $P|_{\omega_1} < P|_{\omega_2}$ . These observations and results suggest that polymeric films on MP substrates have a final thickness  $h_f$  comparable to the substrate roughness in agreement to X-ray results and the literature [50]. Other films on the CMP substrate (Figure 5c,d) and self-standing (S-S, Figure 5e) are featureless and do not need additional morphological descriptions.

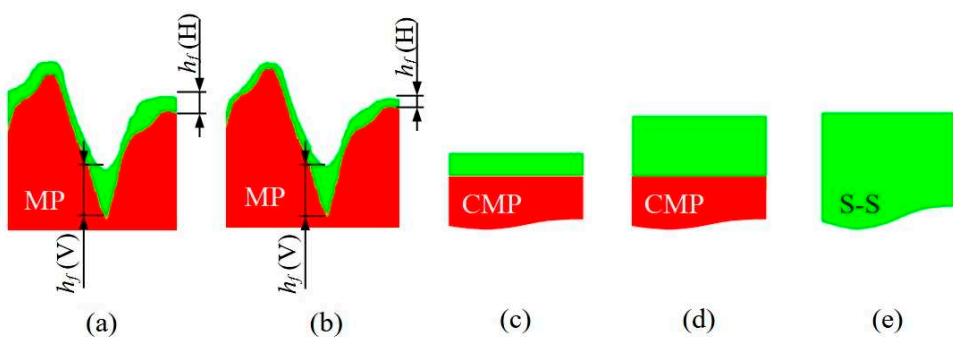


**Figure 5.** Sketches of solid films (green regions) cross-sections obtained by: spin-coating on MP substrates (red regions) at  $\omega = 3500$  rpm (a) and 4000 rpm; (c) spin-coating on CMP substrates (c); (d) drop-casting on CMP substrates; and (e) casting on Teflon Petri dish (self-standing film – S-S –, cp. to Section 2.4). Polymeric films on MP substrates present several details on valleys,  $h_f(V)$ , and hills,  $h_f(H)$ , due to wetting that modulates locally the final film thickness  $h_f$ . On flat regions,  $h_f$  is thicker for low  $\omega$  (a) and thinner for high ones (b), while in valleys it remains constant.

### 3.4. Elastic modulus of polymeric films measured in air

The mechanical properties of polymeric films were measured by FVM [51,52]. Raw force-height curves composing the FVM were vertically aligned to the  $x$ -axis (baseline subtraction,  $y = 0$ ) and horizontally shifted to the  $y$ -axis by setting the height value to  $x = 0$  at  $F = 0$ , i.e. where the tip-sample interaction starts to be in repulsive regime (also termed “contact point”, the measured height is therefore rescaled). To perform quantitative measurements of mechanical properties, force-height curves have to be converted into force-tip-sample separation (TSS) curves [53] by subtracting the bending of the cantilever to the height (see Figure 6a). As reported by Cappella [28], the approach curve is used to measure indentation  $\delta$  and elastic modulus  $E$ , while the retraction curve is used to measure the adhesion force  $F_{adh}$  and the work required to separate the tip from the sample, i.e. the work of adhesion  $W_{adh}$  (see Figure 6a).

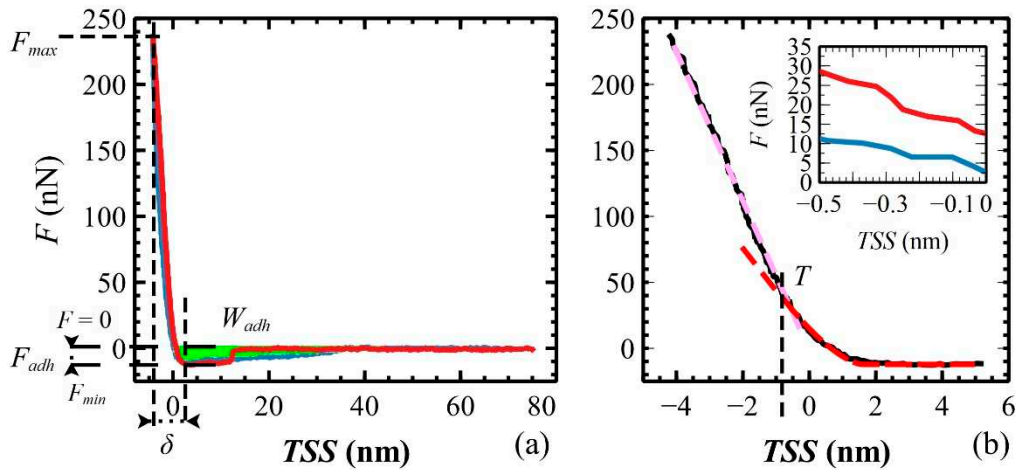


**Figure 6.** (a) Typical force  $F$  vs. Tip Sample Separation (TSS) obtained on polymeric films with all measurable parameters:  $F_{max}$ ,  $F_{adh}$ ,  $\delta$  and  $W_{adh}$ ; (b) Zoom of the approach curve in the tip-sample contact region. In the first few nm, from 5 to -2 nm, the sample is plastically deformed by the tip and Hertz model fits properly the curve (red dashed line). Then, the sample begins to be plastically deformed at point  $T$ , where the curve changes its slope (pink dashed line). Inset: Zoom of  $F$  vs. TSS curve near  $TSS = 0$  for highlighting the small curve hysteresis symptomatic of an elastoplastic behavior of the film.

To measure  $E$  of polymeric films the Hertz model was adopted wherein the tip is approximated to a sphere. This approximation is valid for a tip indentation  $\delta$  smaller than the radius of curvature of the tip  $\Xi$ . In these experiments,  $\Xi = 10$  nm is calculated by averaging the maximum nominal  $\Xi$  reported in datasheets (12, 12 and 8 nm for Bruker RTEP, LTEP and MikroMash NSC35, respectively), so  $\delta < \Xi$  for all measurements (Table 3). The choice of the Hertz model is also validated by the adhesion force  $F_{adh}$  measured as the difference between the minimum force,  $F_{min}$ , and the baseline, i.e.  $F = 0$  (see Figure 6a) [54,55]. The calculation of  $E$  through the Hertz model is precise if the maximum applied force  $F_{max}$  is much larger than  $F_{adh}$  [56–58]. In our films,  $F_{adh}$  runs from a minimum of  $\approx 6$  nN (CMP-DC sample) to a maximum of  $\approx 19$  nN (CMP-SC sample) with  $F_{max} \approx 120$  nN and  $\approx 260$  nN, respectively (see Table 3). The ratio  $F_{adh}/F_{max}$  is within the range [0.05, 0.07] hence  $E$  is measured correctly.

**Table 3.** Sample properties extracted from *F-TSS* curves analysis: tip indentation  $\delta$ , maximum force exercises by the tip  $F_{max}$ , adhesion force  $F_{adh}$  and work of separation  $W_{sep}$  [59].

Sample	$\delta$ (nm)	$F_{max}$ (nN)	$F_{adh}$ (nN)	$W_{sep}$ ( $\cdot 10^{-17}$ J)	$E$ (GPa)
MP-SC	$1.6 \pm 0.3$	$121 \pm 5$	$14 \pm 1$	$6.8 \pm 0.7$	$12 \pm 6$
CMP-SC	$2.6 \pm 0.5$	$257 \pm 4$	$16.8 \pm 1.6$	$8 \pm 1$	$12 \pm 4$
CMP-DC	$4.2 \pm 0.3$	$120.4 \pm 0.6$	$7.7 \pm 0.1$	$3.6 \pm 0.8$	$3.2 \pm 0.5$
S-S	$5.8 \pm 0.5$	$240 \pm 1$	$8.2 \pm 1.6$	$3.3 \pm 0.6$	$2.8 \pm 0.7$

The inset of Figure 6b shows a small hysteresis between the approach and retraction curves, typical of an elastoplastic deformation of the films [28]. The indentation  $\delta$ , measured as the difference between *TSS* values at  $F_{min}$  and  $F_{max}$  (see Figure 6a) [60], shows two slopes indicated by two dashed lines in Figure 6b. The portion of the approach curve from the  $F_{min}$  plateau to the intersection  $T$  is the elastic deformation of the film, useful to measure  $E$  (first few nm, the red dashed line is the fitting curve obtained by using the Hertz model). Then, the film is plastically deformed by the tip for additional few nm, as indicated by the pink dashed line (guide to the eye) [61]. The last parameter adopted in the Hertz model fitting is the Poisson' ratio of polymeric films  $\nu$  that is fixed to 0.33 from the literature [62]. This choice is supported by experimental results on similar amorphous polymeric films (see SI of Ref. [62]) where the magnitude of  $E$  shows slight changes within a realistic  $\nu$  interval, i.e.  $0 < \nu < 0.5$  and, also, the trend of  $E$  vs. film thickness  $h_f$  is preserved for all  $\nu$ .

As shown in Figure 7, thicker films have comparable  $E$  ( $\approx 3$  GPa, see Table 3), in agreement with the results obtained on similar bulk films (1-10  $\mu\text{m}$  thick) [64]. Our polymeric films reach the bulk value for  $h_f \geq 200$  nm, independently of  $c$  (S-S and CMP-DC were obtained from solutions with  $c = 4$  and 1  $\text{mg}\cdot\text{ml}^{-1}$ , respectively). For ultra-thin films,  $E$  increases to  $\approx 12$  GPa with a variance of  $\approx 0.3$  and  $\approx 7$  for CMP-SC and MP-SC, respectively. Due to the high variance,  $E$  for MP-SC samples spans from  $\approx 7$  to  $\approx 20$  GPa, suggesting that  $h_f$  is locally not homogeneous by reason of the high local roughness  $R_{q1}$  with respect to the flatness of CMP substrates.

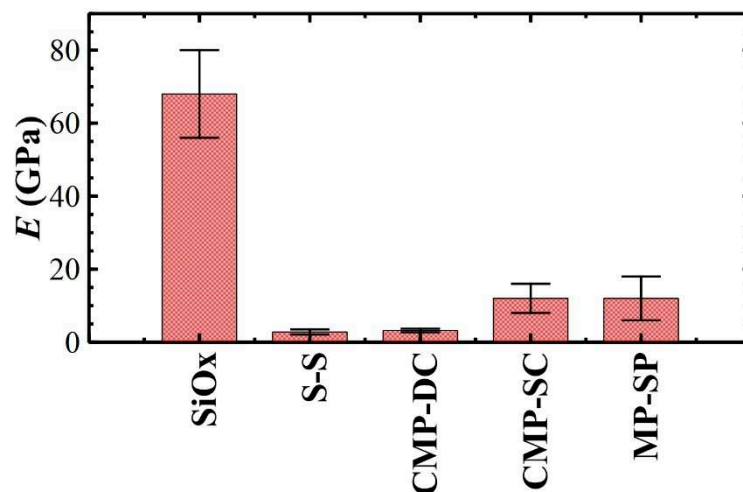


**Figure 7.** Young moduli  $E$  of polymeric films deposited by casting, drop-casting (DC) and spin-coating (SC) on CMP and MP substrates, except for self-standing films (S-S). Such values are compared to  $E$  of SiO<sub>x</sub> [63].

The film thickness  $h_f$  plays a key role in the  $E$  interpretation;  $E$  is accurate if the ratio  $\delta/h_f \leq 0.025$  (film-affected zone) otherwise it is overestimated if  $\delta/h_f > 0.15$  (substrate-dominated zone).

CMP-DC and S-S films are  $\approx 200$  nm and  $\approx 400$   $\mu\text{m}$  thick, respectively. The tip indentation  $\delta$  is  $\approx 4$  and  $\approx 6$  nm obtained by applying a maximum force  $F_{max}$  of  $\approx 120$  nN and  $\approx 240$  nN, respectively (see Table 3). S-S samples are definitely in the film-affected zone because  $\delta/h_f \approx 1.5 \cdot 10^{-5}$ . Similarly, CMP-DC samples have  $\delta/h_f \approx 0.02$ , hence in both cases  $E$  measurements are accurate. In the case of ultra-thin films prepared by spin-coating on CMP and MP substrates,  $E$  was measured in flat regions

between MP substrate scratches, which are morphologically similar to flat CMP substrates (but with higher roughness). CMP-SC films are flat with constant thickness  $h_f \approx 12$  nm;  $\delta$  is  $\approx 2.6$  nm by applying  $F_{max}$  of  $\approx 260$  nN, so  $\delta/h_f \approx 0.22 > 0.15$  and  $E$  is overestimated (substrate-dominated zone). In MP-SC samples, ultra-thin films are thinner than those prepared on CMP substrates because they are deposited at higher rotational speed ( $\omega = 3500$  rpm compared to  $\omega = 3200$  rpm). The thickness  $h_f$  is  $< 12$  nm,  $\delta$  is  $\approx 1.6$  nm for  $F_{max} \approx 120$  nN and  $\delta/h_f > 0.13$  (at minimum). This value of  $\delta/h_f$  is between film- and substrate-dominated zones (transition zone), but the measured  $E$  is comparable to CMP-SC samples therefore MP-SC samples are in substrate-dominated zone. Such overestimation of  $E$  on ultra-thin films is reported in the literature [64–67], and it is associated with the supporting substrate [65] and the polymer molecular weight [68]. In addition, it can also be explained by using an extreme case-study termed “contact-induced stiffening” [69], i.e. when the substrate is elastically deformed by the tip after a fully plastic deformation of the film [55].

The adhesion between the tip and the sample increases for increasing interaction time, i.e. for increasing indentation  $\delta$  [70]. This phenomenon is due to the increase of the effective surface area of the tip interacting with the sample, resulting in an increase of the overall adhesion between the tip and the sample. During sample indentation (approach curve), the tip interacts with the sample by van der Waals forces and H-bond [71]. The sum of such interactions increase with increasing effective surface area therefore the adhesion force  $F_{adh}$  is expected to increase with an increase in the maximum applied force  $F_{max}$  (see Table 3) [70]. Once indentation is complete, the tip is retracted from the surface (retraction curve) and the work to detach the tip from the sample (adhesion work, in J) is the work necessary to break van der Waals forces and H-bond (material dependent), and then to overcome capillary forces [72]. As shown in Table 3,  $F_{adh}$  and  $W_{adh}$  depend on film thickness with higher values for ultra-thin films possibly because their thickness is close to the critical one ( $\approx 10$  nm) [73]. By comparing data in Table 3 with the literature,  $F_{adh}$  is comparable to the one obtained on PMMA films [74] suggesting that MMA branches might be exposed at the film surface.

### 3.5. Elastic modulus of polymeric films measured in liquid

When polymeric films are immersed in mQ water, a certain amount of water is soaked up into the film over time. As shown in Figure 8,  $E$  decreases exponentially for increasing immersion time  $t_i$  with a time constant  $t_0$ , defining the minimum soaked time after which the mechanical properties of wet samples saturate to  $E_s$  [75]. As expected,  $t_0$  and  $E_s$  depend on the thickness  $h_f$  (see Table 4): i) ultra-thin films show a shorter minimum soaked time  $t_0 \approx 0.37$  h (Figure 8a) with respect to thick and thin films that take more time to soak up water,  $t_0 \approx 2.65$  h (Figure 8b); ii) wet samples reduce their elastic modulus by about 92 % and notably by 98 % for S-S samples. By comparing ultra-thin and thin films deposited on the same substrate, *viz.* CMP-SC and CMP-DC samples,  $E_s$  for the former is about four times larger than the latter (see Table 4), and thus the  $E$  ratio observed in air is preserved in water (cp. to Table 3).

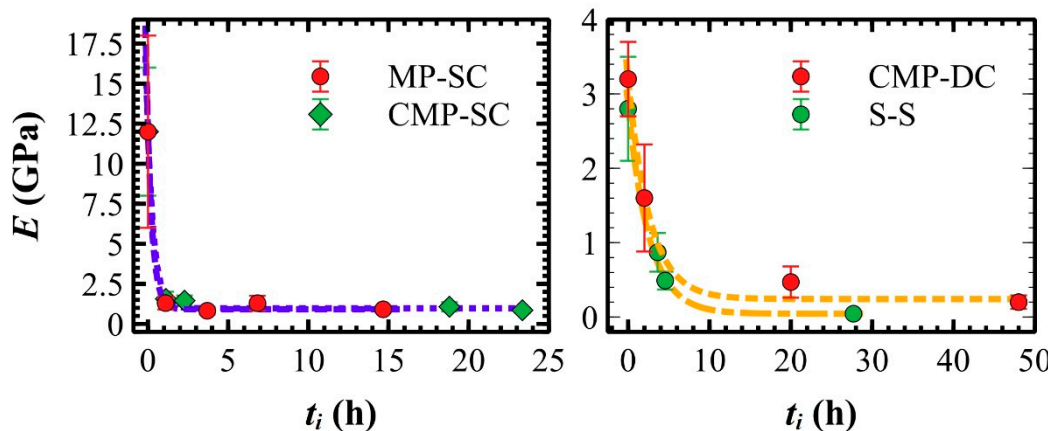


**Figure 8.** Exponential decay (dashed lines) of  $E$  vs  $t_i$  for thin (a) and thick (b) films. For convenience,  $t_i$  measured in sexagesimal was converted in centesimal.

**Table 4.** Mechanical properties of films immersed in water.

Sample	$t_0$ (h)	$E_s$ (GPa)	$F_{adh}$ (nN)	$W_{adh}$ ( $\cdot 10^{-17}$ J)
MP-SC	$0.33 \pm 0.08$	$0.91 \pm 0.09$	$0.7 \pm 0.2$	$1.1 \pm 0.3$
CMP-SC	$0.41 \pm 0.13$	$0.97 \pm 0.15$	$0.8 \pm 0.2$	$1.3 \pm 0.3$
CMP-DC	$2.7 \pm 0.8$	$0.24 \pm 0.1$	$1.3 \pm 0.6$	$1.2 \pm 0.5$
S-S	$2.6 \pm 0.3$	$0.044 \pm 0.005$	$0.7 \pm 0.3$	$1.1 \pm 0.3$

Films on CMP substrates were used to test how indentation  $\delta$  changes for a fixed immersion time ( $t_i \approx 2$  h). In air, CMP-SC films show a  $\delta$  of  $\approx 2.6$  nm by applying a maximum force  $F_{max}$  of  $\approx 260$  nN whereas, after  $\approx 2$  h of immersion, the same indentation ( $\delta \approx 2.8$  nm) is obtained with one fifth of the force ( $F_{max} \approx 45$  nN). On CMP-DC films,  $\delta$  is doubled after  $t_i \approx 2$  h, increasing from  $\approx 5.8$  nm (in air) to  $\approx 10.6$  nm (in water) by applying half of the force (240 vs 110 nN). Such mechanical behavior is caused by the films swelling [76]. On featureless surfaces like CMP-SC and CMP-DC samples, swelling is observable only by X-ray or ellipsometry measurements [76,77] whereas a surface rich of morphological features is necessary for AFM measurements [78]. This is the case of MP-SC samples that are characterized in flat regions between deep scratches (cp. Section 3.3) where swelling depends on the substrate morphology: it is large in flat regions and small within scratches due to the confinement effect of scratch walls [79,80]. Such local film expansions produce an increase of the surface roughness  $R_q$  for all immersion times [80,81]. The roughness grows and saturates following an exponential saturating curve characterized by a time constant  $t_R = (0.44 \pm 0.16)$  (Figure 9, blue dashed line). Thanks to *in situ* FVMs, the same topographic profile crossing a deep scratch ( $> 20$  nm, taken as reference) was collected in two consecutive FVM at  $t_i \approx 1.03$  and 1.1 h, i.e. where  $R_q$  starts to saturate. As shown in the inset of Figure 9, film swelling in the flat region is clearly visible. *In situ* FVMs performed in liquid confirm also that the film is water-insoluble (see sequence of images in Figure 9) [7]. As expected in liquid [72],  $F_{adh}$  and  $W_{adh}$  are largely reduced and constant for all samples within experimental errors (see Table 4), confirming that capillary forces give the main contribution to the tip-sample adhesion.

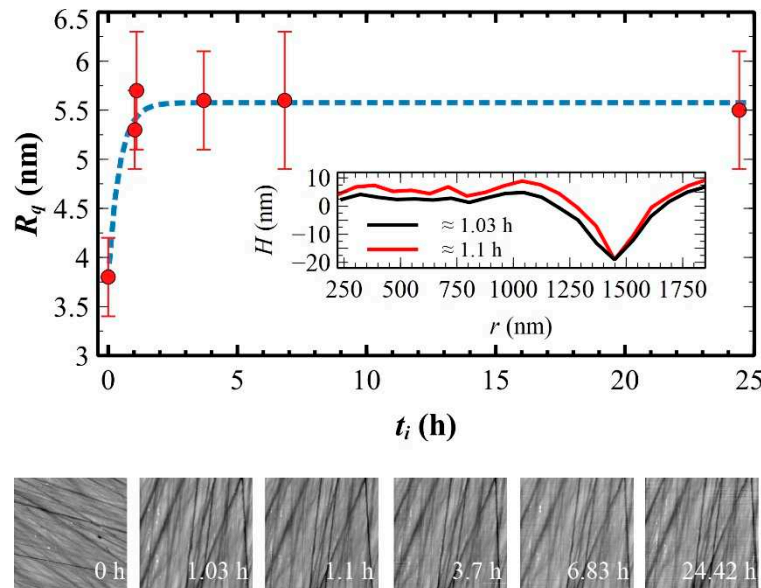


**Figure 9.** Exponential growth of  $R_q$  vs  $t_i$ . The  $R_q$  value at  $t_i = 0$  was measured in air on the same sample but not *in situ*. For convenience,  $t_i$  measured in sexagesimal was converted in centesimal. Inset: Cross-sections across a flat region measured in the same position of the surface from two consecutive images

(1.03 and 1.1 h). Below: Sequence of topographic images collected for increasing  $t_i$  in the same position (*in situ*, except the first one at  $t_i = 0$ ).

In view of these results, the morphological interpretation reported in the introduction and envisaged in Ref. [6] appears to be correct. Swelling of the star copolymer network causes a stretching of the A, B and C components. Depending on the cross-link density, the network architecture, and the polymer–solvent interaction, the swelling equilibrium is reached at different amounts of solvent uptake [80], making film softer at the surface or in the first 10 nm at most. Notably, the minimum soaked time  $t_0$  for thick films (2.65 h) includes the 1.5 h for having high effectiveness of antimicrobial activity due to charges [7] and the stress time of bacteria membranes [12]. Lastly, the large reduction of  $E$  for S-S samples might promotes a conformal contact between bacteria and film, thus enhancing all chemical/physical phenomena related to antimicrobial activity.

#### 4. Conclusions

Star copolymer films with antimicrobial activity were produced by spin-coating, drop-casting and casting deposition techniques obtaining ultra-thin, thin and thick films, respectively. Thin and thick films are morphologically flat, while ultra-thin films have a morphology dependent on the substrate. In the case of a rough substrate, polymer films smoothed the substrate surface except for (relatively) deep scratches. Mechanical properties of such films were investigated by FVMs in both air and liquid. In air, ultra-thin films are in the substrate-dominated zone and thus the elastic modulus  $E$  is overestimated, while  $E$  reaches its bulk value for thin and thick films, specifically for thicknesses  $> 200$  nm. Surface adhesion is correlated to the film thickness showing larger adhesion in ultra-thin films with respect to thin and thick films. In liquid (water),  $E$  follows an exponential decay for all films with a minimum soaked time  $t_0$  of 0.37 and 2.65 h for ultra-thin and thin and thick films, respectively. After this time,  $E$  saturates to a value that is reduced by about 92 % or more for all films. Such films softening is caused by swelling. These results are consistent with the morphological picture envisaged in Ref. [6] and, moreover, seems suggest a role of mechanical properties in the antimicrobial activity. Since  $t_0$  are short with respect to the timescale of standard FVMs, Fast Force Mapping Mode [82] is indispensable for investigating the first two hours of the swelling process that are crucial for understanding changes in mechanical properties.

**Supplementary Materials:** The following supporting information can be downloaded at the website of this paper posted on Preprints.org, Figure S1: Viscosity  $\eta_0$  of the A(BC)<sub>2</sub> solution vs. the mass fraction  $x$  of A(BC)<sub>2</sub> dissolved in the solution.; Figure S2: Intersections of adjacent peaks and valleys (purple horizontal lines) for a typical MP topographic profile.

**Author Contributions:** Conceptualization, C.A., L.I. and F.B.; methodology, C.A.; validation, C.A.; formal analysis, C.A.; investigation, C.A. G.V. and F.L.; resources, L.I., G.V. and F.B.; data curation, C.A. and F.L.; writing—original draft preparation, C.A. and F.L.; writing—review and editing, C.A., L.I., G.V. and F.B. All authors have read and agreed to the published version of the manuscript.

**Funding:** This research received no external funding.

**Data Availability Statement:** Not applicable.

**Acknowledgments:** C.A. wish to thank Maria Letizia Focarete, Francesco Valle and Marco Brucale for useful suggestions and discussions and John B. Stephen for proofreading the manuscript. Data were analysed by the GNU General Public Licensed Software QtiPlot and figures are prepared by the GNU General Public Licensed Software Veusz.

**Conflicts of Interest:** The authors declare no conflict of interest.

#### References

1. Gorrasi, G.; Stanzione, M.; Izzo, L. Synthesis and Characterization of Novel Star-like PEO-PMMA Based Copolymers. *React. Funct. Polym.* **2011**, *71*, 23–29, doi:10.1016/j.reactfunctpolym.2010.11.007.
2. Choi, Y.K.; Bae, Y.H.; Kim, S.W. Star-Shaped Poly(Ether-Ester) Block Copolymers: Synthesis, Characterization, and Their Physical Properties. *Macromolecules* **1998**, *31*, 8766–8774, doi:10.1021/ma981069i.

3. Izzo, L.; Pappalardo, D. "tree-Shaped" Copolymers Based on Poly(Ethylene Glycol) and Atactic or Isotactic Polylactides: Synthesis and Characterization. *Macromol. Chem. Phys.* **2010**, *211*, 2171–2178, doi:10.1002/macp.201000347.
4. Yang, Y.; Chen, M.; Li, H.; Li, H. The Degree of Crystallinity Exhibiting a Spatial Distribution in Polymer Films. *Eur. Polym. J.* **2018**, *107*, 303–307, doi:10.1016/j.eurpolymj.2018.08.041.
5. Wu, W.; Wang, W.; Li, J. Star Polymers: Advances in Biomedical Applications. *Prog. Polym. Sci.* **2015**, *46*, 55–85, doi:10.1016/j.progpolymsci.2015.02.002.
6. Vigliotta, G.; Mella, M.; Rega, D.; Izzo, L. Modulating Antimicrobial Activity by Synthesis: Dendritic Copolymers Based on Nonquaternized 2-(Dimethylamino)Ethyl Methacrylate by Cu-Mediated ATRP. *Biomacromolecules* **2012**, *13*, 833–841, doi:10.1021/bm2017349.
7. Matrella, S.; Vitiello, C.; Mella, M.; Vigliotta, G.; Izzo, L. The Role of Charge Density and Hydrophobicity on the Biocidal Properties of Self-Protonable Polymeric Materials. *Macromol. Biosci.* **2015**, *15*, 927–940, doi:10.1002/mabi.201400503.
8. Francolini, I.; Ruggeri, V.; Martinelli, A.; D'Ilario, L.; Piozzi, A. Novel Metal-Polyurethane Complexes with Enhanced Antimicrobial Activity. *Macromol. Rapid Commun.* **2006**, *27*, 233–237, doi:10.1002/marc.200500786.
9. Sun, Y.; Sun, G. Novel Refreshable N-Halamine Polymeric Biocides: Grafting Hydantoin-Containing Monomers onto High Performance Fibers by a Continuous Process. *J. Appl. Polym. Sci.* **2003**, *88*, 1032–1039, doi:10.1002/app.11772.
10. Mella, M.; Mollica, L.; Izzo, L. Influence of Charged Intramolecular Hydrogen Bonds in Weak Polyelectrolytes: A Monte Carlo Study of Flexible and Extendible Polymeric Chains in Solution and near Charged Spheres. *J. Polym. Sci. Part B Polym. Phys.* **2015**, *53*, 650–663, doi:10.1002/polb.23680.
11. Mella, M.; Izzo, L. Structural Properties of Hydrophilic Polymeric Chains Bearing Covalently-Linked Hydrophobic Substituents: Exploring the Effects of Chain Length, Fractional Loading and Hydrophobic Interaction Strength with Coarse Grained Potentials and Monte Carlo Simulations. *Polymer (Guildf.)* **2010**, *51*, 3582–3589, doi:10.1016/j.polymer.2010.05.013.
12. Izzo, L.; Matrella, S.; Mella, M.; Benvenuto, G.; Vigliotta, G. Escherichia Coli as a Model for the Description of the Antimicrobial Mechanism of a Cationic Polymer Surface: Cellular Target and Bacterial Contrast Response. *ACS Appl. Mater. Interfaces* **2019**, *11*, 15332–15343, doi:10.1021/acsami.9b02903.
13. Stanford Nanofabrication Facility Cleaving Wafers and Substrates Available online: <https://www.youtube.com/watch?v=IRoIXjxIcBQ>.
14. Xia, J.; Yu, J.; Lu, S.; Huang, Q.; Xie, C.; Wang, Z. Surface Morphology Evolution during Chemical Mechanical Polishing Based on Microscale Material Removal Modeling for Monocrystalline Silicon. *Materials (Basel)* **2022**, *15*.
15. Tyona, M.D. A Comprehensive Study of Spin Coating as a Thin Film Deposition Technique and Spin Coating Equipment. *Adv. Mater. Res.* **2013**, *2*, 181–193, doi:10.12989/amr.2013.2.4.181.
16. Mella, M.; Tagliabue, A.; Vaghi, S.; Izzo, L. Evidences for Charged Hydrogen Bonds on Surfaces Bearing Weakly Basic Pendants: The Case of PMMA-Ran-PDMAEMA Polymeric Films. *Colloids Surfaces A Physicochem. Eng. Asp.* **2021**, *620*, 126525, doi:10.1016/j.colsurfa.2021.126525.
17. Exstrand, C.W. Spin Coating of Very Thin Polymer Films. *Polym. Eng. Sci.* **1994**, *34*, 390–394, doi:10.1002/pen.760340503.
18. Meyerhofer, D. Characteristics of Resist Films Produced by Spinning. *J. Appl. Phys.* **1978**, *49*, 3993–3997, doi:10.1063/1.325357.
19. Koryta, J. *Diffusion. Mass Transfer in Fluid Systems*; Cambridge university press, 1985; Vol. 194; ISBN 0521871212.
20. Bornside, D.E.; Macosko, C.W.; Scriven, L.E. Spin Coating of a PMMA/Chlorobenzene Solution. *J. Electrochem. Soc.* **1991**, *138*, 317–320, doi:10.1149/1.2085563.
21. Hall, D.B.; Underhill, P.; Torkelson, J.M. Spin Coating of Thin and Ultrathin Polymer Films. *Polym. Eng. Sci.* **1998**, *38*, 2039–2045, doi:10.1002/pen.10373.
22. Bank, D.D. Vapor Pressure of Chloroform Available online: [http://www.ddbst.com/en/EED/PCP/VAP\\_C47.php](http://www.ddbst.com/en/EED/PCP/VAP_C47.php).
23. Chang, C.C.; Pai, C.L.; Chen, W.C.; Jenekhe, S.A. Spin Coating of Conjugated Polymers for Electronic and Optoelectronic Applications. *Thin Solid Films* **2005**, *479*, 254–260, doi:10.1016/j.tsf.2004.12.013.
24. Cavallini, M.; Albonetti, C.; Biscarini, F. Nanopatterning Soluble Multifunctional Materials by Unconventional Wet Lithography. *Adv. Mater.* **2009**, *21*, 1043–1053.
25. Sader, J.E.; Chon, J.W.M.; Mulvaney, P. Calibration of Rectangular Atomic Force Microscope Cantilevers. *Rev. Sci. Instrum.* **1999**, *70*, 3967–3969, doi:10.1063/1.1150021.
26. Smolyakov, G.; Formosa-Dague, C.; Severac, C.; Duval, R.E.; Dague, E. High Speed Indentation Measures by FV, QI and QNM Introduce a New Understanding of Bionanomechanical Experiments. *Micron* **2016**, *85*, 8–14, doi:10.1016/j.micron.2016.03.002.
27. Garcia, R. Nanomechanical Mapping of Soft Materials with the Atomic Force Microscope: Methods, Theory and Applications. *Chem. Soc. Rev.* **2020**, *49*, 5850–5884, doi:10.1039/d0cs00318b.

28. Cappella, B.; Dietler, G. Force-Distance Curves by Atomic Force Microscopy. *Surf. Sci. Rep.* **1999**, *34*, 1–104, doi:[http://dx.doi.org/10.1016/S0167-5729\(99\)00003-5](http://dx.doi.org/10.1016/S0167-5729(99)00003-5).

29. Chiodini, S.; D'Avino, G.; Muccioli, L.; Bartolini, L.; Gentili, D.; Toffanin, S.; Albonetti, C. Self-Organization of Complete Organic Monolayers via Sequential Post-Deposition Annealing. *Prog. Org. Coatings* **2020**, *138*, 105408, doi:<https://doi.org/10.1016/j.porgcoat.2019.105408>.

30. D'Costa, N.P.; Hoh, J.H. Calibration of Optical Lever Sensitivity for Atomic Force Microscopy. *Rev. Sci. Instrum.* **1995**, *66*, 5096–5097, doi:10.1063/1.1146135.

31. Bruker Corporation JPK Bio-Compatible Glue Available online: <https://www.bruker.com/en/products-and-solutions/microscopes/bioafm/bioafm-accessories/jpk-bio-compatible-glue.html>.

32. Nečas, D.; Klapetek, P. Gwyddion: An Open-Source Software for SPM Data Analysis. *Cent. Eur. J. Phys.* **2012**, *10*, 181–188, doi:10.2478/s11534-011-0096-2.

33. Gualtieri, E.; Pugno, N.; Rota, A.; Spagni, A.; Lepore, E.; Valeri, S. Role of Roughness Parameters on the Tribology of Randomly Nano-Textured Silicon Surface. *J. Nanosci. Nanotechnol.* **2011**, *11*, 9244–9250, doi:10.1166/jnn.2011.4296.

34. Technologies, P. *Abrasive Grinding Paper*; 2011;

35. Gadelmawla, E.S.; Koura, M.M.; Maksoud, T.M.A.; Elewa, I.M.; Soliman, H.H. Roughness Parameters. *J. Mater. Process. Technol.* **2002**, *123*, 133–145, doi:10.1016/S0924-0136(02)00060-2.

36. Dagnall, H. *Exploring Surface Texture*; Rank Taylor Hobson, 1986; ISBN 090192007X.

37. De, R.R.L.; Albuquerque, D.A.C.; Cruz, T.G.S.; Yamaji, F.M.; Leite, F.L. Measurement of the Nanoscale Roughness by Atomic Force Microscopy: Basic Principles and Applications. In *Atomic Force Microscopy - Imaging, Measuring and Manipulating Surfaces at the Atomic Scale*; Bellitto, V., Ed.; IntechOpen: Rijeka, 2012; p. Ch. 7.

38. Simpson, G.J.; Sedin, D.L.; Rowlen, K.L. Surface Roughness by Contact versus Tapping Mode Atomic Force Microscopy. *Langmuir* **1999**, *15*, 1429–1434, doi:10.1021/la981024a.

39. Wu, W.; Wallace, W.E. <title>Characterization of Planarity of Polymer Thin Films on Rough Surfaces</Title>. *Scatt. Surf. Rough. II* **1998**, *3426*, 222–228, doi:10.1117/12.328458.

40. Garoff, S.; Sirota, E.B.; Sinha, S.K.; Stanley, H.B. The Effects of Substrate Roughness on Ultrathin Water Films. *J. Chem. Phys.* **1989**, *90*, 7505–7515, doi:10.1063/1.456184.

41. Wu, P.; Chou, F. Complete Analytical Solutions of Film Planarization during Spin Coating. *J. Electrochem. Soc.* **1999**, *146*, 3819–3826, doi:10.1149/1.1392558.

42. Precision Devices, I. Surface Roughness Terminology and Parameters Available online: [www.predev.com/pdffiles/surface\\_roughness\\_terminology\\_and\\_parameters.pdf](http://www.predev.com/pdffiles/surface_roughness_terminology_and_parameters.pdf).

43. Wei, J.; Verhaar, T.M.; Sarro, P.M. Pattern Transfer on a Vertical Cavity Sidewall Using SU8. *J. Micromechanics Microengineering* **2009**, *19*, 74018, doi:10.1088/0960-1317/19/7/074018.

44. Stillwagon, L.E.; Larson, R.G.; Taylor, G.N. Planarization of Substrate Topography by Spin Coating. *J. Electrochem. Soc.* **1987**, *134*, 2030–2037, doi:10.1149/1.2100813.

45. Park, S.; Tsarkova, L.A. Surface Roughness-Mediated Ordering in Block Copolymer Films toward Spatially Controlled Patterns. *Macromolecules* **2017**, *50*, 6840–6848, doi:10.1021/acs.macromol.7b01185.

46. Zheng, W.; Yu, X.; Jin, Y. Considering Surface Roughness Effects in a Triangular Pore Space Model for Unsaturated Hydraulic Conductivity. *Vadose Zo. J.* **2015**, *14*, 1–13, doi:10.2136/vzj2014.09.0121.

47. C. Grant Willson Spincoating Available online: [https://willson.cm.utexas.edu/Research/Sub\\_Files/Planarization/simulation.php](https://willson.cm.utexas.edu/Research/Sub_Files/Planarization/simulation.php) (accessed on 4 September 2023).

48. Valle, F.; Brucale, M.; Chiodini, S.; Bystrenova, E.; Albonetti, C. Nanoscale Morphological Analysis of Soft Matter Aggregates with Fractal Dimension Ranging from 1 to 3. *Micron* **2017**, *100*, 60–72, doi:10.1016/j.micron.2017.04.013.

49. Henry, C.; Minier, J.P.; Lefèvre, G. Numerical Study on the Adhesion and Reentrainment of Nondeformable Particles on Surfaces: The Role of Surface Roughness and Electrostatic Forces. *Langmuir* **2012**, *28*, 438–452, doi:10.1021/la203659q.

50. Yu, Z.; Hwu, J.; Liu, Y.; Gauzner, G.; Lee, K.; Kuo, D. Study of Spin-Coated Resist Coverage on Nanoscale Topography Using Spectroscopic Ellipsometry. *J. Appl. Phys.* **2011**, *110*, 14303, doi:10.1063/1.3603019.

51. Hoffman, D. Measuring the Elastic Modulus of Polymers Using the Atomic Force Microscope. **2010**, *43*.

52. Olubowale, O.H.; Biswas, S.; Azom, G.; Prather, B.L.; Owoso, S.D.; Rinee, K.C.; Marroquin, K.; Gates, K.A.; Chambers, M.B.; Xu, A.; et al. "may the Force Be with You!" Force-Volume Mapping with Atomic Force Microscopy. *ACS Omega* **2021**, *6*, 25860–25875, doi:10.1021/acsomega.1c03829.

53. Franz, C.M.; Taubnerberger, A.; Puech, P.H.; Muller, D.J. Studying Integrin-Mediated Cell Adhesion at the Single-Molecule Level Using AFM Force Spectroscopy. *Sci. STKE* **2007**, *2007*, pl5–pl5, doi:10.1126/stke.4062007pl5.

54. Lin, Z.; Yu, Z.; Wei, Y. Measurement of Nanoindentation Properties of Polymers Considering Adhesion Effects between AFM Sharp Indenter and Material. *J. Adhes. Sci. Technol.* **2020**, *34*, 1591–1608, doi:10.1080/01694243.2020.1714117.

55. Zak, S.; Trost, C.O.W.; Kreiml, P.; Cordill, M.J. Accurate Measurement of Thin Film Mechanical Properties Using Nanoindentation. *J. Mater. Res.* **2022**, *37*, 1373–1389, doi:10.1557/s43578-022-00541-1.

56. Dokukin, M.E.; Sokolov, I. On the Measurements of Rigidity Modulus of Soft Materials in Nanoindentation Experiments at Small Depth. *Macromolecules* **2012**, *45*, 4277–4288, doi:10.1021/ma202600b.

57. Tranchida, D.; Piccarolo, S.; Soliman, M. Nanoscale Mechanical Characterization of Polymers by AFM Nanoindentations: Critical Approach to the Elastic Characterization. *Macromolecules* **2006**, *39*, 4547–4556, doi:10.1021/ma052727j.

58. Griepentrog, M.; Krämer, G.; Cappella, B. Comparison of Nanoindentation and AFM Methods for the Determination of Mechanical Properties of Polymers. *Polym. Test.* **2013**, *32*, 455–460, doi:10.1016/j.polymertesting.2013.01.011.

59. Bruker QI<sup>TM</sup> Makes AFM Easy - Perfect for Non-Experts, Beginners and Occasional Users Available online: <https://www.jpk.com/products/atomic-force-microscopy/qi-mode/pid4448> (accessed on 18 September 2023).

60. Butt, H.-J.; Cappella, B.; Kappl, M. Force Measurements with the Atomic Force Microscope: Technique, Interpretation and Applications. *Surf. Sci. Rep.* **2005**, *59*, 1–152, doi:<https://doi.org/10.1016/j.surprep.2005.08.003>.

61. Chang, Y.R.; Raghunathan, V.K.; Garland, S.P.; Morgan, J.T.; Russell, P.; Murphy, C.J. Automated AFM Force Curve Analysis for Determining Elastic Modulus of Biomaterials and Biological Samples. *J. Mech. Behav. Biomed. Mater.* **2014**, *37*, 209–218, doi:10.1016/j.jmbbm.2014.05.027.

62. Stafford, C.M.; Vogt, B.D.; Harrison, C.; Julthongpitud, D.; Huang, R. Elastic Moduli of Ultrathin Amorphous Polymer Films. *Macromolecules* **2006**, *39*, 5095–5099, doi:10.1021/ma060790i.

63. Bassous, E. Fabrication of Novel Three-Dimensional Microstructures by the Anisotropic Etching of (100) and (110) Silicon. *IEEE Trans. Electron Devices* **1978**, *25*, 1178–1185, doi:10.1109/T-ED.1978.19249.

64. Miyake, K.; Satomi, N.; Sasaki, S. Elastic Modulus of Polystyrene Film from near Surface to Bulk Measured by Nanoindentation Using Atomic Force Microscopy. *Appl. Phys. Lett.* **2006**, *89*, 31925, doi:10.1063/1.2234648.

65. Geng, K.; Yang, F.; Druffel, T.; Grulke, E.A. Nanoindentation Behavior of Ultrathin Polymeric Films. *Polymer (Guildf)* **2005**, *46*, 11768–11772, doi:10.1016/j.polymer.2005.08.096.

66. Oommen, B.; Van Vliet, K.J. Effects of Nanoscale Thickness and Elastic Nonlinearity on Measured Mechanical Properties of Polymeric Films. *Thin Solid Films* **2006**, *513*, 235–242, doi:10.1016/j.tsf.2006.01.069.

67. Dimitriadis, E.K.; Horkay, F.; Maresca, J.; Kachar, B.; Chadwick, R.S. Determination of Elastic Moduli of Thin Layers of Soft Material Using the Atomic Force Microscope. *Biophys. J.* **2002**, *82*, 2798–2810, doi:10.1016/S0006-3495(02)75620-8.

68. Torres, J.M.; Stafford, C.M.; Vogt, B.D. Impact of Molecular Mass on the Elastic Modulus of Thin Polystyrene Films. *Polymer (Guildf)* **2010**, *51*, 4211–4217, doi:10.1016/j.polymer.2010.07.003.

69. Liu, H.; Liu, W.; Fujie, T.; Nakajima, K. Contact-Induced Stiffening in Ultrathin Amorphous Polystyrene Films. *Polymer (Guildf)* **2018**, *153*, 521–528, doi:10.1016/j.polymer.2018.08.050.

70. Viville, P.; Deffieux, A.; Schappacher, M.; Leclère, P.; Brédas, J.L.; Lazzaroni, R. Influence of Tip Indentation Depth on the Adhesive Behavior of Viscoelastic Polydimethylsiloxane Networks Studied by Atomic Force Microscopy. *Macromol. Symp.* **2001**, *167*, 189–199, doi:10.1002/1521-3900(200103)167:1<189::AID-MASY189>3.0.CO;2-2.

71. Rezende, C.A.; Lee, L.T.; Galembeck, F. Surface Mechanical Properties of Thin Polymer Films Investigated by AFM in Pulsed Force Mode. *Langmuir* **2009**, *25*, 9938–9946, doi:10.1021/la9010949.

72. Weisenhorn, A.L.; Hansma, P.K.; Albrecht, T.R.; Quate, C.F. Forces in Atomic Force Microscopy in Air and Water. *Appl. Phys. Lett.* **1989**, *54*, 2651–2653, doi:10.1063/1.101024.

73. Tanaka, K.; Takahara, A.; Kajiyama, T. Film Thickness Dependence of the Surface Structure of Immiscible Polystyrene/Poly(Methyl Methacrylate) Blends. *Macromolecules* **1996**, *29*, 3232–3239, doi:10.1021/ma951140+.

74. Jiang, Y.; Turner, K.T. Measurement of the Strength and Range of Adhesion Using Atomic Force Microscopy. *Extrem. Mech. Lett.* **2016**, *9*, 119–126, doi:10.1016/j.eml.2016.05.013.

75. Chen, J.; Hu, H.; Li, S.; He, Y. Evolution of Mechanical Properties of Polypropylene Separator in Liquid Electrolytes for Lithium-Ion Batteries. *J. Appl. Polym. Sci.* **2018**, *135*, 46441, doi:10.1002/app.46441.

76. Singh, A.; Mukherjee, M. Swelling Dynamics of Ultrathin Polymer Films. *Macromolecules* **2003**, *36*, 8728–8731, doi:10.1021/ma034583j.

77. Ogieglo, W.; Wormeester, H.; Eichhorn, K.J.; Wessling, M.; Benes, N.E. In Situ Ellipsometry Studies on Swelling of Thin Polymer Films: A Review. *Prog. Polym. Sci.* **2015**, *42*, 42–78, doi:10.1016/j.progpolymsci.2014.09.004.

78. Benaglia, S.; Drakopoulou, S.; Biscarini, F.; Garcia, R. In Operando Nanomechanical Mapping of PEDOT:PSS Thin Films in Electrolyte Solutions with Bimodal AFM. *Nanoscale* **2022**, *14*, 14146–14154, doi:10.1039/d2nr02177c.

79. Vasil'eva, V.I.; Kranina, N.A.; Malykhin, M.D.; Akberova, E.M.; Zhiltsova, A. V. The Surface Inhomogeneity of Ion-Exchange Membranes by SEM and AFM Data. *J. Surf. Investig.* **2013**, *7*, 144–153, doi:10.1134/S1027451013010321.
80. Metze, F.K.; Sant, S.; Meng, Z.; Klok, H.A.; Kaur, K. Swelling-Activated, Soft Mechanochemistry in Polymer Materials. *Langmuir* **2023**, *39*, 3546–3557, doi:10.1021/acs.langmuir.2c02801.
81. Bonaccorso, E.; Graf, K. Nanostructuring Effect of Plasma and Solvent Treatment on Polystyrene. *Langmuir* **2004**, *20*, 11183–11190, doi:10.1021/la036441o.
82. Murphy, J.G.; Raybin, J.G.; Ansay, G.E.; Sibener, S.J. Spatiotemporal Mapping of Hole Nucleation and Growth during Block Copolymer Terracing with High-Speed Atomic Force Microscopy. *ACS Nano* **2023**, *17*, 5644–5652, doi:10.1021/acsnano.2c11672.

**Disclaimer/Publisher's Note:** The statements, opinions and data contained in all publications are solely those of the individual author(s) and contributor(s) and not of MDPI and/or the editor(s). MDPI and/or the editor(s) disclaim responsibility for any injury to people or property resulting from any ideas, methods, instructions or products referred to in the content.